

## Chapter 2

# Simulation Overview

**Abstract** MRI Simulator is based on numerical solution of the Bloch Equation. The numerical solution is obtained as a time update form of the magnetization vector. Parameters of this time update coefficients are shown to be related to the pulse sequence parameters and gradient amplitudes. The contents include application of the time update solution for simulation of Gradient Echo (GRE) sequences. Influence of  $T2^*$  and susceptibility effects are also discussed.

**Keywords** Bloch equation • MRI simulator •  $T2^*$  effect • SWI

Image quality of MRI, acquired using multiple phased array coils is often dictated by spatially varying noise and large geometry factors. For dynamic acquisitions such as cardiac and functional MRI (fMRI), the image quality is affected by subject movements, leading to geometric distortions. Further, in phase sensitive acquisition such as PC-MRA, the influence of noise mostly affects computations performed on phase images. The nature and influence of different types of noise sources can only be understood and remedial algorithms developed with the possibility of simulating the actual scanning process.

MR Simulator uses electrical and magnetic fields from electromagnetic field calculations to simulate realistic MR Images. The accuracy of simulator increases with the accuracy of model generated and its characteristics [1]. For example, it is possible to simulate spatial diffusion by convolving the time-dependent magnetization with a kernel representative of Gaussian diffusion. Apart from simulation of unrestricted diffusion, the convolution approach is also employed to model steady-state free precession [2] and gradient spoiling for steady-state sequences [3]. In an alternative form of simulation, the phenomenon of intra-voxel dephasing is simulated using Bloch-Torrey equation [4]. This involves an additional term in the Bloch equation that describes signal losses due to the diffusion process. The use of Bloch-Torrey equation for simulation of magnetization vectors allows more efficient simulation compared to that using spatial summation of isochromats. The technique is most applicable to simulating the effect of field perturbations,

i.e. intra-voxel dephasing, but also for other typical imaging experiments and simulation of diffusion weighting [4]. Dephasing due to unrestricted motion such as blood flow could be simulated by incorporating voxel-dependent velocity and acceleration [5]. Bloch Equations, in general, compute temporal dynamics of the net magnetization. The Bloch MR Simulator can be implemented using realistic simulation of spatial field variation due to gradients and RF field effects in MRI.

## 2.1 Bloch Equation

Bloch equation provides a phenomenological description of the time dependence of magnetization. The solution of Bloch equation involves computation of magnetization vector  $\vec{M} = (M_x, M_y, M_z)$  as a function of time. Magnetization along each cartesian direction is represented by the respective vector component along x, y, and z directions. For deriving the Bloch equation, the magnetic spin is assumed to be placed in a static magnetic field  $B_0$ , in the z direction. The magnetic moments orient either along field direction, or it's opposite. It causes the spins to precess at the Larmor frequency  $\omega_0 = \gamma B_0$ . Equation governing the dynamics of magnetization vector  $\vec{M}$  in the static magnetic field is described using

$$\frac{d\vec{M}}{dt} = \gamma \vec{M} \times \vec{B}_0 \hat{k} \quad (2.1)$$

where  $\times$  represents cross product indicating that the rate of change of  $\vec{M}$  is perpendicular to both  $\vec{M}$  and  $\vec{B}_0$ . This implies that the initial spin precession is about the direction of the main magnetic field. Measuring the intensity of magnetization vector is practically impossible due to dominance of the external field  $B_0$ . In order to change the plane of precession, the magnetization  $\vec{M}$  is tipped towards the transverse x-y plane. The factors affecting relaxation of the magnetization vector  $\vec{M}$ , are the relaxation time constants  $T_1$  and  $T_2$  [6, 7]. The spin-lattice relaxation time  $T_1$  corresponds to the time required for the system to return to its equilibrium value after it has been exposed to a  $90^\circ$  tipping pulse. The spin-spin relaxation time  $T_2$  depicts the time required for the tipped magnetization in the x-y plane to decay down to zero. The differential equation for magnetization in the presence of a magnetic field with relaxation terms can be combined to form a vector differential equation. In vectorized form, the Bloch equation becomes

$$\frac{d\vec{M}}{dt} = \gamma \vec{M} \times \vec{B}_{ext} + \frac{1}{T_1} (M_0 - M_z) \hat{k} - \frac{1}{T_2} (M_x \hat{i} + M_y \hat{j}) \quad (2.2)$$

where  $B_{ext} = B_0 \hat{k}$  and  $\vec{M} = M_x \hat{i} + M_y \hat{j} + M_z \hat{k}$ . Since the external field components are zero along x and y directions, the cross product term will be  $M_y B_0 \hat{i} - M_x B_0 \hat{j}$ . Substituting the cross product terms into (2.2) gives

$$\begin{aligned} \frac{d}{dt} \left( M_x \hat{i} + M_y \hat{j} + M_z \hat{k} \right) = & \gamma (M_y B_0 \hat{i} - M_x B_0 \hat{j}) + \frac{1}{T_1} (M_0 - M_z) \hat{k} \\ & - \frac{1}{T_2} (M_x \hat{i} + M_y \hat{j}) \end{aligned} \quad (2.3)$$

Equating the coefficients of  $\hat{i}$ ,  $\hat{j}$  and  $\hat{k}$  on both sides,

$$\frac{dM_z}{dt} = \frac{M_0 - M_z}{T_1} \quad (2.4)$$

$$\frac{dM_x}{dt} = \omega_0 M_y - \frac{M_x}{T_2} \quad (2.5)$$

$$\frac{dM_y}{dt} = \omega_0 M_x - \frac{M_y}{T_2} \quad (2.6)$$

### 2.1.1 Solution of Bloch Equation

Equation (2.4) is similar to the standard first-order differential equation,  $\frac{dy}{dx} + P(x)y = Q(x)$ ; whose solution is directly obtained as  $y \left( e^{\int P dx} \right) = \int Q e^{\int P dx} dx$ . Substituting  $P = \frac{1}{T_1}$  and  $Q = \frac{M_0}{T_1}$ , the solution of (2.4) takes the form

$$M_z(t) = M_0 + C e^{-t/T_1} \quad (2.7)$$

Solving for  $C$  in terms of the initial longitudinal magnetization at  $t = 0$ , the time dependent form of the longitudinal magnetization will be

$$M_z(t) = M_z(0) e^{-t/T_1} + M_0 (1 - e^{-t/T_1}) \quad (2.8)$$

To solve (2.5) and (2.6), the transverse magnetizations are assumed to be exponential in nature; each relaxing with time constant  $T_2$ .

$$\begin{aligned} M_x &= m_x e^{\frac{-t}{T_2}} \\ \text{and} \\ M_y &= m_y e^{\frac{-t}{T_2}} \end{aligned} \quad (2.9)$$

From (2.9), we get  $\frac{dM_x}{dt} = \frac{m_x}{T_2}$  and  $\frac{dM_y}{dt} = \frac{m_y}{T_2}$ . Substituting for  $M_x$ ,  $M_y$ ,  $\frac{dM_x}{dt}$  and  $\frac{dM_y}{dt}$  into (2.5) and (2.6),

$$\frac{dM_x}{dt} = \omega_0 m_y e^{\frac{-t}{T_2}} - \frac{m_x}{T_2} e^{\frac{-t}{T_2}} \quad (2.10)$$

and

$$\frac{dM_y}{dt} = \omega_0 m_x e^{\frac{-t}{T_2}} - \frac{m_y}{T_2} e^{\frac{-t}{T_2}} \quad (2.11)$$

Comparing (2.10) and (2.11) with (2.5) and (2.6),

$$\begin{aligned} \frac{dm_x}{dt} &= \omega_0 m_y \\ \text{and} \\ \frac{dm_y}{dt} &= -\omega_0 m_x \end{aligned} \quad (2.12)$$

Differentiating (2.12) once again,

$$\frac{d^2 m_x}{dt^2} = \omega_0 \frac{dm_y}{dt} \quad (2.13)$$

Substituting for  $\frac{dm_y}{dt}$  from (2.12), (2.13) becomes

$$\begin{aligned} \frac{d^2 m_x}{dt^2} &= \omega_0 (-\omega_0 m_x) \\ &= -\omega_0^2 m_x \end{aligned} \quad (2.14)$$

Since (2.14) is a standard form of second-order differential equation, its solution is easily obtained as

$$m_x = C_1 \cos(\omega_0 t) + C_2 \sin(\omega_0 t) \quad (2.15)$$

Noting (2.9) through (2.15), the solution for time varying magnetization is

$$\begin{aligned} M_x &= e^{\frac{-t}{T_2}} (C_1 \cos(\omega_0 t) + C_2 \sin(\omega_0 t)) \\ \text{and} \\ M_y &= e^{\frac{-t}{T_2}} (-C_1 \sin(\omega_0 t) + C_2 \cos(\omega_0 t)) \end{aligned} \quad (2.16)$$

Considering the initial values of  $M_x$  and  $M_y$  to be  $M_x(0)$  and  $M_y(0)$ , the unknown constants  $C_1$  and  $C_2$  can be evaluated. For a constant field  $B_{ext} = B_0 \hat{k}$  in the longitudinal direction, the final form of solution of the Bloch equation will be

$$\vec{M}(t) = \begin{bmatrix} M_z(0)e^{-t/T_1} + M_0(1 - e^{-t/T_1}) \\ e^{\frac{j}{2}\omega_0 t}(M_x(0) \cos(\omega_0 t) + M_y(0) \sin(\omega_0 t)) \\ e^{\frac{j}{2}\omega_0 t}(M_y(0) \cos(\omega_0 t) - M_x(0) \sin(\omega_0 t)) \end{bmatrix} \quad (2.17)$$

### 2.1.2 Time Update Form of Bloch Equation

The Bloch equation in the rotating frame is computed by time updated computation of spin magnetization vector at each spatial location in the x-y plane of the selected slice. For any pulse sequence, the spin precession frequency in the rotating frame of reference is changed by application of external spatial encoding gradients. The effect of RF tipping is simulated as a hard pulse that tips each spatial magnetization vector into the x-y plane. Following application of the hard pulse, strength of the initial magnetization is computed using

$$M_0 = \frac{\rho_0 \gamma^2 \hbar^2}{4kT} (B_0 + \Delta B_0) \quad (2.18)$$

where  $\rho_0$  is the proton density,  $\gamma$  is the gyromagnetic ratio,  $\hbar$  is the Plank's constant,  $k$  is the Boltzmann constant,  $T$  is the tissue temperature,  $B_0$  is the main magnetic field and  $\Delta B_0$  is the static field inhomogeneity. Once the initial magnetization is computed using (2.20), the Bloch equation is solved by stepping forward through time, while approximating the evolution of each magnetization vector using

$$\vec{M}(\vec{r}, t + \Delta t) = Rot_z(\theta_g) \cdot Rot_z(\theta_{iH}) \cdot R_{relax} \cdot R_{RF} \cdot \vec{M}(\vec{r}, t) \quad (2.19)$$

Here,  $\theta_g$  and  $\theta_{iH}$  denote the phase accumulated due to the applied time-varying gradient, and field inhomogeneities respectively.  $Rot_z(\theta)$  represents the rotation matrix used to represent rotation of the tipped magnetization vector about z-axis by an angle  $\theta$ .

$$Rot_z(\theta) = \begin{bmatrix} \cos \theta & \sin \theta & 0 \\ -\sin \theta & \cos \theta & 0 \\ 0 & 0 & 1 \end{bmatrix} \quad (2.20)$$

In a given time interval  $\Delta t$ , the angle of precession is determined by the sum of angular components contributed by the spin precession frequencies due to the applied gradients  $\theta_g = \omega_y \Delta t$  and local field inhomogeneities  $\theta_{iH} = \gamma \Delta B \Delta t$  respectively. If the applied gradients are time varying, the phase accumulated in a given time interval  $\Delta t$  is given by

$$\theta_g = \gamma \int_t^{t+\Delta t} (xG_x(\tau) + yG_y(\tau)) d\tau \quad (2.21)$$

The matrix  $R_{relax}$  describes the effects of transverse and longitudinal relaxations [8]. The diagonal elements of this matrix indicate the change in signal magnitudes due to relaxations in the x, y and z components respectively.

$$R_{relax} = \begin{bmatrix} e^{\frac{-\Delta t}{T_2(\vec{r})}} & 0 & 0 \\ 0 & e^{\frac{-\Delta t}{T_2(\vec{r})}} & 0 \\ 0 & 0 & 1 - e^{\frac{-\Delta t}{T_1(\vec{r})}} \end{bmatrix} \quad (2.22)$$

If the assumption of a hard pulse is not considered, the RF pulse combines the effect of rotations about z-axis, and flipping about the x or y axis. With the application of a circularly polarized RF pulse:  $B_{RF} = B_1(\cos(\omega t) + j \sin(\omega t))$  to tip the magnetization by a flip angle  $\alpha$ , the combined effects of rotation and flip are represented using the matrix

$$R_{RF} = Rot_z(\omega_1 t) \cdot Rot_x(\alpha) \cdot Rot_z(-\omega_1 t) \quad (2.23)$$

where  $\omega_1 = \gamma B_1$ . In the case where the local field differs from  $B_0$  due to field inhomogeneity or chemical shift effects, the resonance frequency  $\omega_{RF}$  deviates from  $\omega_0$  as defined in (1.1). Consequently, the effective precessional frequency becomes

$$\omega_{eff} = \sqrt{(\omega_{RF} - \omega_0)^2 + \omega_1^2} \quad (2.24)$$

A  $B_1$  pulse of duration  $\tau_p$  tips  $\vec{M}$  by an angle  $\alpha$  from  $B_0$ , resulting in an effective flip angle

$$\alpha_{eff} = \tau_p \sqrt{(\omega_{RF} - \omega_0)^2 + \left(\frac{\alpha}{\tau_p}\right)^2} \quad (2.25)$$

## 2.2 Working Principle of MR Simulator

MRI head phantom forming input to the simulator, consists of individual spatial maps representative of the tissue relaxation parameters, proton density etc. In specific imaging applications, additional parametric maps may be called for. For example, in Susceptibility Weighted Imaging (SWI), this corresponds to a map of intrinsic susceptibility variations. In PC-MRA, the same parametric maps are used to differentiate vascular regions from background tissue.

Once the required input parametric maps are provided, the simulator solves the Bloch equation using the time-update form, and computes the spin magnetization vector at each spatial position in the transverse (x-y) plane of a given slice [7–10]. By applying a  $90^\circ$  hard pulse along the phase-encode direction, the Free Induction Decay (FID) signals in the *inphase* and *quadrature* coils are obtained as the x and y components of the magnetization vector at each time point. A complex signal is then formed by treating the x-component as the real part, and y-component as the imaginary part. The time update solution is formulated by combining effects of precession and relaxation in each time interval. In matrix form, the time-update form of solution is

$$\vec{M}(t + \Delta t) = \mathbf{A}\vec{M}(t) + \mathbf{B} \quad (2.26)$$

where the matrix parameters  $\mathbf{A}$  and  $\mathbf{B}$  are determined from  $Rot_z(\theta)$  and  $R_{relax}$  as

$$\mathbf{A} = \begin{bmatrix} e^{-\Delta t/T_2} & 0 & 0 \\ 0 & e^{-\Delta t/T_2} & 0 \\ 0 & 0 & e^{-\Delta t/T_1} \end{bmatrix} \begin{bmatrix} \cos \theta & \sin \theta & 0 \\ -\sin \theta & \cos \theta & 0 \\ 0 & 0 & 1 \end{bmatrix}$$

and

$$\mathbf{B} = \begin{bmatrix} 0 \\ 0 \\ 1 - e^{-\Delta t/T_1} \end{bmatrix} \quad (2.27)$$

As discussed in Sect. 2.1.2, the precession angle  $\theta$  is computed using the product of off-resonance frequency  $\Delta\omega$  and time-interval  $\Delta t$ . The off-resonance frequency pertaining to a frequency-encoding pulse of constant amplitude  $G_x$  is given by

$$\Delta\omega = \frac{\gamma x G_x}{2\pi} \quad (2.28)$$

The net magnetization is obtained by summing up the spatial magnetizations from allocations in the transverse plane [11–13]. Application of a phase-encoding gradient pulse of amplitude  $\Delta G_y$  and duration  $\tau$  adds a phase  $\varphi$  to the FID signal originating from spatial location  $P(x, y)$ . Based on the y-location, the encoded phase at  $P(x, y)$  is determined as

$$\varphi = \frac{\gamma y \Delta G_y \tau}{2\pi} \quad (2.29)$$

Implementation of the simulator requires specification of the echo and repetition times ( $TE$  and  $TR$ ) and also the flip angle ( $\alpha$ ). The sequence type includes information whether the target image is two or three dimensional. For a 2D image, the slice position and orientation is specified. Volumetric acquisition should specify whether the whole FOV is scanned as one thick volume, or as a series of thin slabs.

### 2.2.1 Imaging Parameters and K-Space Generation

Prior to scanning, all MR imaging sequences require specification of the FOV and required image resolution. The FOVs are separately specified in the x and y directions as  $FOV_x$  and  $FOV_y$  respectively. The image resolution is specified using the number of voxels in the x and y directions, with the y-direction typically being the phase-encoding direction. For an axial scan, the phase-encode typically corresponds to the Anterior-Posterior (AP) direction, and the frequency-encoding from the Left-Ear to Right-Ear (LR) respectively. The sampling intervals in the frequency and phase-encode directions are

$$\begin{aligned}\Delta k_x &= \frac{1}{FOV_x} \\ \Delta k_y &= \frac{1}{FOV_y}\end{aligned}\tag{2.30}$$

Also, from the Fourier imaging principle described in Sect. 1.3, the k-space sampling intervals are also related to the frequency and phase-encode pulse amplitudes using

$$\begin{aligned}\Delta u &= \frac{\gamma G_x \Delta t}{2\pi} \\ \Delta v &= \frac{\gamma \Delta G_y \tau}{2\pi}\end{aligned}\tag{2.31}$$

Noting (2.30) through (2.31), the step-size for phase encoding is obtained as

$$\Delta G_y = \frac{2\pi}{\gamma \tau FOV_y}\tag{2.32}$$

The entire k-space is filled by varying the amplitude of phase-encoding pulse using integral multiples of  $\Delta G_y$ . For M phase-encoding steps,

$$G_y = \begin{cases} -\frac{M}{2}\Delta G_y \text{ to } (\frac{M}{2}-1)\Delta G_y, & \text{for } M \text{ even,} \\ -\frac{(M+1)}{2}\Delta G_y \text{ to } (\frac{M+1}{2})\Delta G_y, & \text{for } M \text{ odd.} \end{cases}\tag{2.33}$$

Each spatial frequency component ( $k_x, k_y$ ) is represented by an individual data point  $S(\vec{k})$  in the k-space as discussed in Chap. 1. The k-space contains complex data with the real part denoting the *inphase* (I), and the imaginary part, the *quadrature* (Q) component of magnetization. Each different combination of the gradient pulses is considered to move the acquisition point in the k-space. Changing the step-size of phase-encoding pulse amplitudes, fills the k-space line-by-line. The procedural steps for MR simulation is summarized in the block schematic shown in Fig. 2.1.



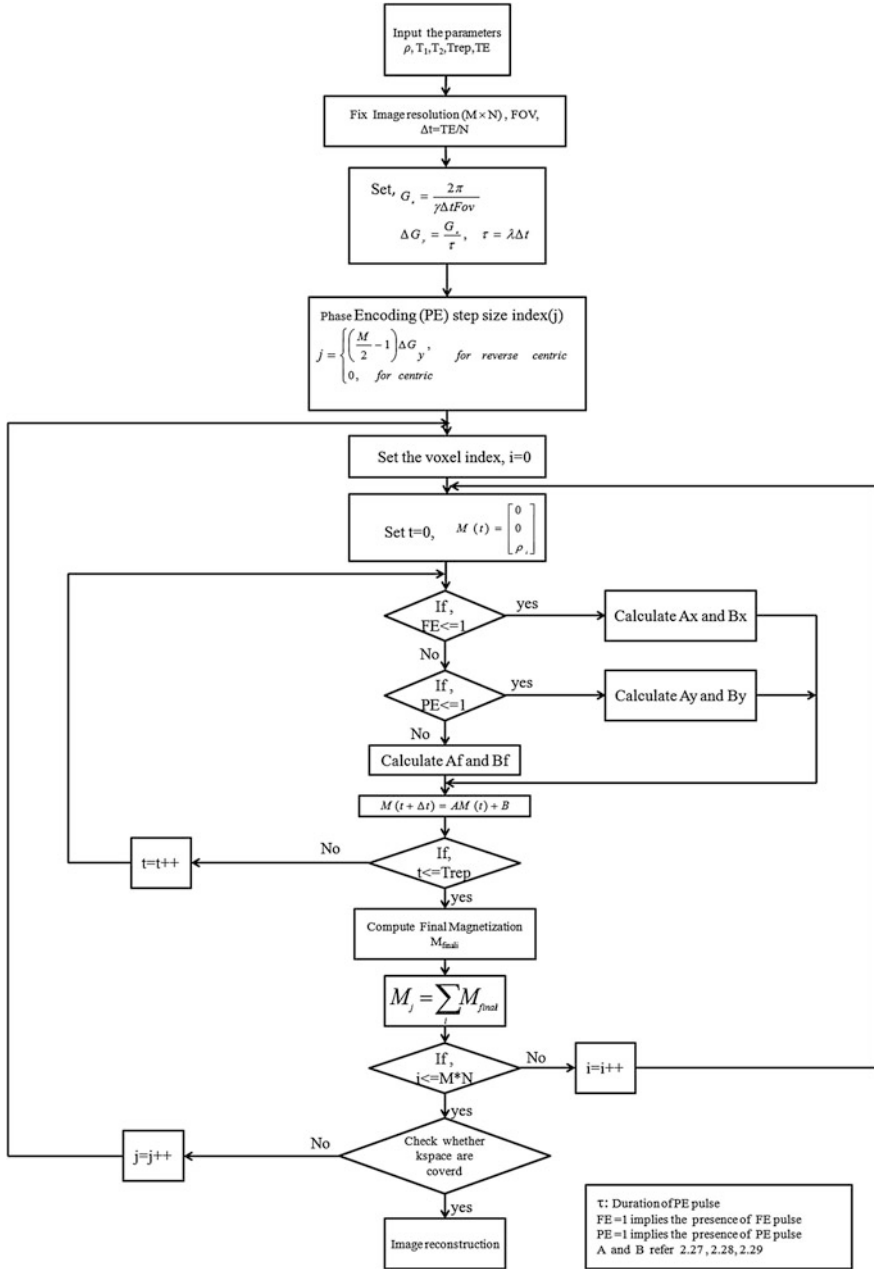


Fig. 2.1 Work flow of MR simulation

### 2.3 Incorporation of $T_2^*$ Effects in Gradient-Echo Imaging

Intra-voxel field inhomogeneities lead to deviations in the transverse decay rate of spins from the same isochromat. The cumulative effect of all spins within the same voxel result in much faster decay rate of transverse magnetizations [14], than would be predicted by natural atomic and molecular mechanisms. The  $T_2^*$  value can be considered as an effective modification of the basic  $T_2$  value of the tissue being imaged.  $T_2^*$  effect essentially originates from inhomogeneities in the main magnetic field. The inhomogeneities arise due to intrinsic defects in the magnet itself, or susceptibility-induced field distortions produced by the tissue. Some MR sequences using gradient-echoes acquired using long TE values are relatively more  $T_2^*$ -weighted. In MR simulation, the  $T_2^*$  effect is mathematically represented by the perturbations of the basic relaxation rate with an additional frequency term generated by the local field inhomogeneity. This is mathematically represented as

$$\frac{1}{T_2^*} = \frac{1}{T_2} + \gamma \Delta B_i \quad (2.34)$$

### 2.4 Incorporation of Susceptibility Effects

The magnetic susceptibility ( $\chi$ ) denotes the degree of magnetization of a material in response to an applied magnetic field. Since the tissues are diamagnetic and concentrations of paramagnetic agents are relatively small, the susceptibility assumes very small values. Once the susceptibility values are known, it is then easy to find a relation between field changes and susceptibility variations.

$$\Delta B = \chi B_0 \quad (2.35)$$

Susceptibility effects [15–17] present in brain tissues, lead to off-resonance frequency shifts in *ppm* range. The *ppm* values are appreciably different for venous and arterial structures. The intrinsic susceptibility effects are responsible for phase changes across vessels. Unlike intrinsic susceptibility changes in the *ppm* scale, the bulk susceptibility changes occur at a relatively larger scale. The bulk susceptibility effects mainly occur at air gaps and border regions where the susceptibility values are practically zero on one side of the border. For simulation of intrinsic susceptibility effects, blood vessels are modeled as long cylinders in which the susceptibility values differ inside and outside. Since phase is directly proportional to the local field, it is possible to visualize the field dependence inside and outside of objects embedded in the background. With  $\chi_i(\chi_e)$  representing the inside (outside) susceptibility of an object, the  $\Delta\chi$  will be equivalent to difference between  $\chi_i$  and  $\chi_e$ . The background shift will then depend on the geometry of the structure.

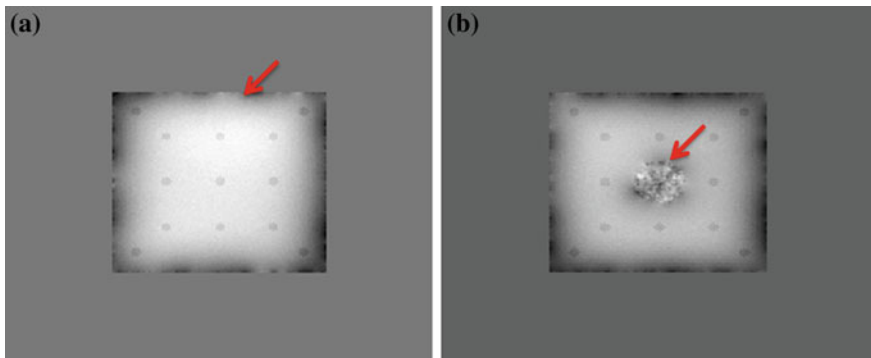


**Fig. 2.2** **a** Simulated phase image without air gap. **b** Simulated phase image with air gap

Consider two analytical phantoms with built in cylindrical structures parallel to the main field ( $z$ -direction). The transverse plane is constructed with a finite resolution ( $256 \times 256$ ), with the cross-section of each cylindrical structure having a radius equivalent to three pixels. The pixels inside the cylinders are assigned a susceptibility value of  $\chi_i = 9.45 \times 10^{-6}$ , and those outside with  $\chi_o = 9 \times 10^{-6}$ . A 3D phantom is then constructed by cascading a number of axial cross-sections, large enough to simulate the effect of an infinitely long cylindrical structure. In a slightly different version of the phantom, a central air gap ( $128 \times 128$ ) is introduced by assigning zero susceptibility in this region. The phase due to spatially varying magnetic field  $B_0$  in both phantoms is calculated from the respective 3D susceptibility maps using [18]

$$\varphi(r) = -\gamma B_0 T E \cdot FT^{-1} \left[ FT(\chi(r)) \cdot \left( \frac{1}{3} - \frac{k_z^2}{k_x^2 + k_y^2 + k_z^2} \right) \right] \quad (2.36)$$

The magnitude images are considered to have uniform intensity in all pixels except zeros in regions containing air gaps. The simulated phase images are shown in Fig. 2.2.

### 2.4.1 Susceptibility Artifacts

Susceptibility artifacts are seen in the magnitude images as dark regions surrounding borders of interfaces having bulk susceptibility changes [19, 20]. The gradients in susceptibility cause dephasing of spins and frequency shifts of the surrounding tissues, resulting in bright and dark areas with spatial distortion of surrounding anatomy. These artifacts are worst for long echo times in gradient-echo

sequences. The susceptibility artifacts can be reduced by performing imaging with low magnetic field strength, smaller voxel size, reduced echo time and increased receiver bandwidth.

SWI uses both phase and magnitude information for the enhancement of venous vasculature. In a typical SWI scan, venous contrast is suppressed in magnitude image due to signal loss in regions with severe field inhomogeneity and peripheral regions with bulk susceptibility changes. SWI processing is performed to enhance the vascular features seen in the magnitude images. The processing, generally involves deriving weights from the high-pass filtered phase image. High-pass filtering is inevitable since it will remove the phase wraps and thereby enhance the high-frequency information. For long echo-times, the magnitude images will have reduced signal intensities due to  $T_2^*$  decay. To simulate the effect of susceptibility artifacts at long echo times, a complex image is generated using the phase synthesized from bulk susceptibility changes and uniform magnitude at all tissue locations.

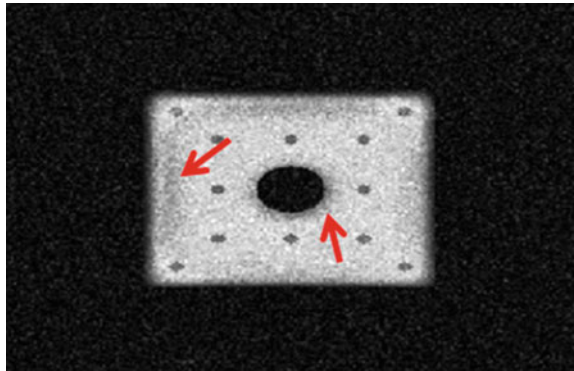
Since vascular information is preserved in the high-frequency phase, SWI processing involves application of a homodyne filter to the phase image. The homodyne filtered phase is given by

$$\theta_{filt} = \text{angle} \left( \frac{I}{FFT^{-1}(h \cdot FFT(I))} \right) \quad (2.37)$$

where  $\theta_{filt}$  is the high-pass filtered phase,  $I$  is the complex image, and  $h$  is a 3D transfer function representing the low-pass filter. The transfer function is a Gaussian low-pass filter. If  $N_i$  corresponds to the number of voxels in the  $i$ th dimension, and  $\sigma$  is a parameter which determines the strength of high-pass filtering, then the filter frequency—response is obtained as

$$H(k_x, k_y, k_z) = \exp \left( - \frac{\left(k_x - \frac{N_x}{2}\right)^2 + \left(k_y - \frac{N_y}{2}\right)^2 + \left(k_z - \frac{N_z}{2}\right)^2}{2\sigma^2} \right) \quad (2.38)$$

**Fig. 2.3** Susceptibility artifact simulated using MATLAB



In SWI processing, the magnitude image is point-filtered using weights derived from the high-pass filtered phase. Relative magnitude of the weights is determined from the difference between internal and external fields at locations occupied by venous elements. If the internal field is larger, then the differences are positive resulting in negative phase values. In this case, the weights decrease from 1 to 0 as the phase values increase from 0 to  $\pi$  in the negative direction. Figure (2.3) shows the magnitude image after application of weights. The susceptibility artifacts are seen as dark patches at the border regions, indicated by the arrows.

## References

1. Haacke EM, Brown RW, Thompson MR, Venkatesan R (1989) Magnetic resonance imaging: physical principles and sequence design. Wiley, New York
2. Cattin HB, Collewet G (2005) Numerical implementation of the Bloch equations to simulate magnetization dynamics and imaging. *J MRI* 173
3. Klepaczko A, Szczypinski P, Dwojakowski G, Strzelecki M, Materka A (2014) Computer simulation of magnetic resonance angiography imaging: model description and validation. *Plosone* 9:e93689
4. Cattin HB, Collewet G, Belaroussi B, Jalmes HS, Odet C (2005) The SIMRI project: a versatile and interactive MRI simulator. *J Mag Res* 173:97–115
5. Jurczuk K, Kretowski BJJ, Eliat PA, Jalmes HS, Wendling JB (2013) Computational modeling of MR flow imaging by the lattice Boltzmann method and Bloch equation. *Mag Res Imaging* 31:1163–1173
6. Jurczuk K, Kretowski M, Eliat PA, Jalmes HS, Wendling JB (2014) *In Silico* modeling of magnetic resonance flow imaging in complex vascular networks. *IEEE Trans Med Imaging* 33:11
7. Kwan RKS, Evans AC, Pike GB (1999) MRI simulation-based evaluation of image-processing and classification methods. *IEEE Trans Med Imaging* 18(11):1085–1097
8. Cao Y, Shen Z, Thomas MA, Chenevert L, Ewing JR (2006) Estimate of vascular permeability and cerebral blood volume using Gd-DTPA contrast enhancement and dynamic T2\*-weighted MRI. *Magn Reson Imaging* 24:288–296
9. Spritzer CE, Pelc NJ, Lee JN, Evans AJ, Sostman HD, Riederer SJ (1999) MRI simulation-based evaluation of image-processing and classification methods. *IEEE Trans Med Imaging* 18:11
10. Bittoun J, Taquin J, Sauzade M (1984) A computer algorithm for the simulation of any nuclear magnetic resonance (NMR) imaging method. *Magn Reson Imaging* 2:113–120
11. Duyn J (2013) MR susceptibility imaging. *JMR* 299:198–207
12. Ruan C. MRI artifacts: mechanism and control. [http://ric.uthscsa.edu/personalpages/lancaster/D12\\_Projects\\_2003/MRI\\_Artifacts.pdf](http://ric.uthscsa.edu/personalpages/lancaster/D12_Projects_2003/MRI_Artifacts.pdf)
13. Bernstein MA, King KF, Zhou XJ (2004) Hand book of MRI pulse sequences. Elsevier Academic Press, Amsterdam
14. Haacke EM, Mittal S, Wu Z, Neelavalli J, Cheng YC (2009) Susceptibility-weighted imaging: technical aspects and clinical applications, Part 1. *AJNR Am J Neuroradiol* 30:19–30
15. Cao Z, Oh S, Sica CT, Mc-Garrity JM, Horan T, Luo W, Collins CM (2014) Bloch-based MRI system simulator considering realistic electromagnetic fields for calculation of signal, noise, and specific absorption rate. *Magn Reson Med* 72:237–247
16. Jochimsen TH, Schaefer A, Bammer R, Moseley ME (2006) Efficient simulation of magnetic resonance imaging with Bloch–Torrey equations using intra-voxel magnetization gradients. *J Magn Reson* 180:29–38

17. Gudbjartsson H, Patz S (1995) Simultaneous calculation of flow and diffusion sensitivity in steady-state free precession imaging. *Magn Reson Med* 34:567–579
18. Marshall I (1999) Simulation of in-plane flow imaging Concepts. *Magn Reson* 11:379–392
19. Yarnykh VL (2010) Optimal radiofrequency and gradient spoiling for improved accuracy of T1 and B1 measurements using fast steady state techniques. *Magn Reson Med* 63:1610–1626
20. Neelavalli J, Cheng YC, Jiang J, Haacke EM (2009) Removing background phase variations in susceptibility-weighted imaging using a fast Forward-Field Calculation. *J Magn Res Imaging* 29:937–948

Understanding Phase Contrast MR Angiography

A Practical Approach with MATLAB examples

Suresh Paul, J.; Gouri Raveendran, S.

2016, VIII, 92 p. 52 illus., 39 illus. in color., Softcover

ISBN: 978-3-319-25481-4